Characterization of EMI Sources from Reconstructed Current Distributions Based on Phase-Less Electric and Magnetic Near-Field Data

Robert Nowak, Anika Henke, Stephan Frei
On-board Systems Lab
TU Dortmund University
Dortmund, Germany
robert.nowak@tu-dortmund.de

***Abstract*—Localization of EMI sources can be a challenging task. The next step is often to identify the parameters of the EMI generating structure and find appropriate suppression. In this work, a method is presented to handle such problems by using only a phase-less scan of the electromagnetic near-field. Here, radiating conductor systems are investigated, like traces on a PCB. Using the electric and/or magnetic near-field distribution, the radiating current distribution can be reconstructed. In this paper an approach based on a known trace geometry and electric as well as magnetic field data is presented. When current distribution is known, critical EMI sources can be found. Furthermore, an approach is presented to design virtually a filter concept for a critical EMI source. For demonstration, based on measurement data, an exemplary conductor structure is investigated. It is pointed out that high currents and high local fields do not necessarily lead to a high far-field. For the exemplary conductor structure, critical sources are identified, and it is shown how the needed filter structures can be found.**

Keywords—current distribution; EMI sources; iterative reconstruction; near-field; phase-less scan; source reconstruction

I. Introduction

Near-field investigations can be very beneficial for root-cause analysis of electromagnetic interferences (EMI). On the one hand, based on the near-field data, the far-field of a structure (e.g. a printed circuit board, PCB) can be estimated without the need of cumbersome antenna measurements [1]. On the other hand, EMI sources can be identified and characterized. For example, the potential influence of an integrated circuit (IC) on other surrounding components can be determined [2]. Here, especially the localization of relevant far-field generating structures is required. If it is possible to get close to the radiating structures currents can be determined using near-field probes or current clamps. So, a prediction of the emitted far-field is possible when the geometry and the material properties of the complete structure are known. However, in many configurations, the radiating structures are not reachable to determine the radiating currents directly. For this, more elaborated methods are necessary. For example, based on the plane-wave spectrum theory, the evaluation of the electric near-field leads to the position of the far-field sources and their quantitative characterization [3]. In [4], the usage of neuronal networks is discussed for the localization of the relevant radiating structures. Both approaches only determine the position of the EMI source but not the parameters of the actual radiating structure. In this paper, based on the reconstruction of the current distribution from phase-less near-field data, an approach is presented to identify the critical radiating structures in a wire system.

To determine the current distribution, measured near-field data can be used. As phase measurements are complex, phase-less data is preferred. Based on the method presented in [5], the introduced current reconstruction method is enhanced significantly in this work. Besides the magnetic near-field, electric near-field data is used for the reconstruction. Similar approaches were already presented in other works. In [6], the relation of the currents and their fields is described by Greens' functions. Another approach, using magnetic and/or electric dipoles and considering electric and magnetic field data, is presented in, e.g., [7]. Both papers use two different field models for the electric field. Here, a third model is added. This quasi-static model is developed and implemented. Also, the approach to consider electric and magnetic field data is different to other works.

This work is a continuation of [5]. In [5], the reconstruction method has only been applied to simulated data. Here, an improved current reconstruction method is used to investigate measured near-field data. Furthermore, the estimation of the termination information presented in [8] is used here. It is shown, how this information can be used to design a filter concept to suppress the emitted field.

The developed method requires information on the wire geometry, propagation constant and wave impedance. It is assumed that all wires are ideal round cables in a homogenous medium (air). Other elements' spatial structure and field emission are neglected. So, sources and terminations are considered as lumped structures. It is assumed that it is known whether the termination networks are passive or active.

After the introduction, the enhanced reconstruction method is presented. Here, the simultaneous consideration of the electric and magnetic near-field data is described. Afterwards, the iterative algorithm developed in [5] is outlined. Here, an approach to improve the initial guess of the phase distribution is presented. Based on this approach, an appropriate condition for the inverse problem of source reconstruction is derived. In the following, the presented method is applied to an exemplary case study object. The reconstruction results for the current distribution are presented. Based on these results, critical field sources are located, and a suitable suppression is designed and discussed. The paper closes with a conclusion and an outlook.

II. Current Reconstruction Method

A. Framework of the Basic Inverse Problem

The current distribution on of a given wire system is the source for the surrounding electromagnetic field. To explain the proposed current reconstruction method, an exemplary

978-1-7281-5579-1/20/$31.00 ©2020 IEEE

structure consisting of three wires above a conducing plane is analyzed. The configuration is shown in Fig. 1. It is assumed that all wires are discretized by N segments for numerical treatment. Every segment n carries a homogenous current I_n. Similar to [5], for each segment current and each observation point, a description of the electric field $\mathbf{E}$ and the magnetic field $\mathbf{H}$ can be found. The superposition the fields from all segments is formulated:

$$[\mathbf{E} \quad \mathbf{H}]^{\mathrm{T}} = [\mathbf{\Psi}_{\mathrm{IE}} \quad \mathbf{\Psi}_{\mathrm{IH}}]^{\mathrm{T}} \cdot \mathbf{I}_{\mathrm{S}}, \qquad \mathbf{I}_{\mathrm{S}} = [I_1 \quad \dots \quad I_{\mathrm{N}}]^{\mathrm{T}} \tag{1}$$

Here, the segment currents are summarized in the vector $\mathbf{I}_{\mathrm{S}}$. The superposition of all electric and magnetic field descriptions is represented in the matrices $\mathbf{\Psi}_{\mathrm{IE}}$ and $\mathbf{\Psi}_{\mathrm{IH}}$. So, the electric and magnetic field data at all observation points is given. Based on the image theory, virtual segments can be considered to model the effect of an infinite perfect electric conducting (PEC) ground plane [9]. Besides, not all components of the electric or magnetic field must be used. If a component is unknown, for example because it was not measured, the corresponding rows in the equation system can be deleted.

As presented in [8], the segment currents in $\mathbf{I}_{\mathrm{S}}$ can be simplified by considering the current distributions along the segments. On the one hand, for a very short section like k_1 in Fig. 1, the assumption of a constant current $I_{\mathrm{c,k_1}}$ is possible:

$$[I_{\mathrm{p,k_1}} \quad \cdots \quad I_{\mathrm{q,k_1}}]^{\mathrm{T}} = [1 \quad \cdots \quad 1]^{\mathrm{T}} \cdot I_{\mathrm{c,k_1}} \tag{2}$$

On the other hand, the transmission-line theory can be used to describe the current distribution in a section. In the following, this is exemplary shown for section k_2 (Fig. 1):

$$\begin{bmatrix} I_{\mathrm{p,k_2}} \\ \vdots \\ I_{\mathrm{q,k_2}} \end{bmatrix} = \begin{bmatrix} \exp\left(-\gamma_{\mathrm{k_2}} d_{\mathrm{p,k_2}}\right) & -\exp\left(\gamma_{\mathrm{k_2}} d_{\mathrm{p,k_2}}\right) \\ \vdots & \vdots \\ \exp\left(-\gamma_{\mathrm{k_2}} d_{\mathrm{q,k_2}}\right) & -\exp\left(\gamma_{\mathrm{k_2}} d_{\mathrm{q,k_2}}\right) \end{bmatrix} \cdot \begin{bmatrix} I_{\mathrm{i,k_2}} \\ I_{\mathrm{r,k_2}} \end{bmatrix} \tag{3}$$

Here, all segment currents of section k_2 are represented by an incident and a reflected current wave $I_{\mathrm{i,k_2}}$ and $I_{\mathrm{r,k_2}}$. Merging all substitutions (i.e. (2) and (3)) in the matrix $\mathbf{\Psi}_{\mathrm{TL}}$, the basic forward problem is given.

$$[\mathbf{E} \quad \mathbf{H}]^{\mathrm{T}} = [\mathbf{\Psi}_{\mathrm{IE}} \quad \mathbf{\Psi}_{\mathrm{IH}}]^{\mathrm{T}} \cdot \mathbf{\Psi}_{\mathrm{TL}} \cdot \mathbf{I} \tag{4}$$

Accordingly, $\mathbf{I}$ contains all incident and reflected current waves plus constant currents to represent the current distribution of the structure.

The formulation (4) is not directly used as our inverse problem. To respect different orders of magnitudes and units, the subproblems for the electric and magnetic field are scaled by the factors α_{E} and α_{H}:

$$[\alpha_{\mathrm{E}}\mathbf{E} \quad \alpha_{\mathrm{H}}\mathbf{H}]^{\mathrm{T}} = [\alpha_{\mathrm{E}}\mathbf{\Psi}_{\mathrm{IE}} \quad \alpha_{\mathrm{H}}\mathbf{\Psi}_{\mathrm{IH}}]^{\mathrm{T}}\mathbf{\Psi}_{\mathrm{TL}}\mathbf{I} \Leftrightarrow \mathbf{F} = \mathbf{\Psi}\mathbf{I} \tag{5}$$

In the resulting formulation, the field data and the forward map are substituted with $\mathbf{F}$ and $\mathbf{\Psi}$. The factors α_{E} and α_{H} are given by the Euclidean norm of the field data according to (6). The factors $\mathcal{N}_{\mathrm{E}}$ and $\mathcal{N}_{\mathrm{H}}$ are defined by the used number of electric and magnetic field components.

$$\text{(a)} \quad \alpha_{\mathrm{E}} = \mathcal{N}_{\mathrm{E}}/\|\mathbf{E}\|_2 \qquad \text{(b)} \quad \alpha_{\mathrm{H}} = \mathcal{N}_{\mathrm{H}}/\|\mathbf{H}\|_2 \tag{6}$$

Using the Euclidean norm, the subproblems of the electric and magnetic field are equally weighted in the inverse problem, as in its solution the norm of the residua is minimized. Using the norm, the subproblems' scaling is more robust against noise in contrast to the usage of maximum values like in [7]. With

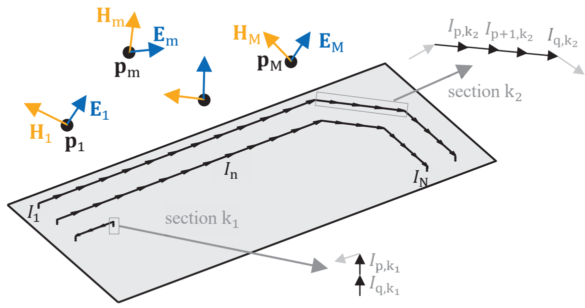

Fig. 1. Exemplary source model generating electric and magnetic fields.

the factors $\mathcal{N}_{\mathrm{E}}$ and $\mathcal{N}_{\mathrm{H}}$, the weighting of the subproblems is corrected to represent the number of recorded data points. Here, for all measurement points, the availability of all used field components is assumed.

Considering the continuity constraints of voltages and currents between the different sections, (5) is solved as an inverse problem. These constraints can be represented by the matrix $\mathbf{K}$ according to [5]. Finally, the following inverse problem results:

$$\hat{\mathbf{I}} = \arg\min_{\tilde{\mathbf{I}}} \left\| \mathbf{\Psi} \cdot \tilde{\mathbf{I}} - \mathbf{F} \right\|_2 \quad \text{such that} \quad \mathbf{K} \cdot \tilde{\mathbf{I}} = \mathbf{0} \tag{7}$$

B. Field Models

Now, the field models are presented to formulate the matrices $\mathbf{\Psi}_{\mathrm{IE}}$ and $\mathbf{\Psi}_{\mathrm{IH}}$. To describe the magnetic field, Hertzian dipoles are used according to [8]. For the electric field, a new model is presented. Neglecting displacement currents, a quasi-static description is applied [9]:

$$\mathbf{E} = -\nabla\varphi - \mathrm{j}\omega\mathbf{A} \tag{8}$$

Based on the electric scalar potential φ and the magnetic vector potential $\mathbf{A}$, the electric field at $\boldsymbol{r} = [x\ y\ z]^{\mathrm{T}}$ is determined using Green's functions [9]:

$$\begin{aligned} &\text{(a)} \quad \mathbf{A} = \frac{\mu}{4\pi} \int_{V_{\mathrm{q}}} \frac{\mathbf{J}(\mathbf{r}_{\mathrm{q}})}{|\mathbf{r} - \mathbf{r}_{\mathrm{q}}|} \mathrm{d}V_{\mathrm{q}} \\ &\text{(b)} \quad \varphi = \frac{1}{4\pi\varepsilon} \int_{V_{\mathrm{q}}} \frac{\rho(\mathbf{r}_{\mathrm{q}})}{|\mathbf{r} - \mathbf{r}_{\mathrm{q}}|} \mathrm{d}V_{\mathrm{q}} \end{aligned} \tag{9}$$

According to the assumption of homogenous segment currents, the integrals are solved. Initially, the current density $\mathbf{J}$ is defined and the charge distribution ρ is determined. Here, the solution for the n-th segment with the length ℓ positioned in the origin of a Cartesian coordinate system along the x-axis is presented exemplary. Based on the current density

$$\mathbf{J}(\mathbf{r}_{\mathrm{q}}) = I_n \cdot \mathrm{rect}(x_{\mathrm{q}}/\ell)\delta(y_{\mathrm{q}})\delta(z_{\mathrm{q}}) \cdot \mathbf{e}_x\,, \tag{10}$$

the charge distribution is determined according to the continuity equation [9]:

$$\begin{aligned} \rho(\mathbf{r}_{\mathrm{q}}) &= -\frac{1}{\mathrm{j}\omega}\nabla \cdot \mathbf{J}(\mathbf{r}_{\mathrm{q}}) \\ &= -\frac{I_{\mathrm{n}}}{\mathrm{j}\omega}\left(\delta\left(x_{\mathrm{q}} + \frac{\ell}{2}\right) - \delta\left(x_{\mathrm{q}} - \frac{\ell}{2}\right)\right)\delta(y_{\mathrm{q}})\delta(z_{\mathrm{q}}) \end{aligned} \tag{11}$$

Thus, using the substitution

$$r^{\pm} = \sqrt{(x \pm \ell/2)^2 + y^2 + z^2}\,, \tag{12}$$

the solutions of (9) and the gradient of φ are:

$$\mathbf{A} = \mathbf{e}_\mathrm{x}\frac{\mu I_n}{4\pi}\operatorname{arsinh}\left(\frac{x+\ell/2}{y^2+z^2}r^- - \frac{x-\ell/2}{y^2+z^2}r^+\right) \tag{13}$$

$$\varphi = -\frac{I_n}{\mathrm{j}\omega\, 4\pi\varepsilon}\left(\frac{1}{r^+}-\frac{1}{r^-}\right) \tag{14}$$

$$\boldsymbol{\nabla}\varphi = \frac{I_n}{\mathrm{j}\omega\, 4\pi\varepsilon}\left(\frac{1}{r^+}\begin{bmatrix} x+\ell/2 \\ y \\ z\end{bmatrix} - \frac{1}{r^-}\begin{bmatrix} x-\ell/2 \\ y \\ z\end{bmatrix}\right) \tag{15}$$

With (13) and (15) the description of the electric field is given by (8). This solution can be applied to each segment by doing geometrical translations and rotations. Using the rotation matrices $\mathbf{R}_{(\cdot)}$, the electric field at $\mathbf{r}_0$ generated by an exemplary segment positioned at $\mathbf{r}_n$ orientated to $\mathbf{e}_\mathrm{s}$ is

$$\begin{aligned} &\mathbf{E} = \mathbf{R}_\mathrm{z}(\phi)\mathbf{R}_\mathrm{y}(\theta)\left(-\boldsymbol{\nabla}\varphi\Big|_{\mathbf{r}=\mathbf{r}_0-\mathbf{r}_n} - \mathrm{j}\omega\,\mathbf{A}\Big|_{\mathbf{r}=\mathbf{r}_0-\mathbf{r}_n}\right) \\ &\text{with } \phi = \operatorname{arctan2}\left(\mathbf{e}_\mathrm{s}\mathbf{e}_\mathrm{y}, \mathbf{e}_\mathrm{s}\mathbf{e}_\mathrm{x}\right) \\ &\text{and } \theta = -\arctan\left(\mathbf{e}_\mathrm{s}\mathbf{e}_\mathrm{z}/\left\|\mathbf{e}_\mathrm{s}\circ\left(\mathbf{e}_\mathrm{x}+\mathbf{e}_\mathrm{y}\right)\right\|_2\right). \end{aligned} \tag{16}$$

Here, the Hadamard product ($\circ$) represents an element-wise product.

C. Solution of the Inverse Problem with Phase-less Near-Field Data

If the near-field is only known by its magnitude (without phase information), an iterative algorithm can be used to determine the solution of the inverse problem. Here, the procedure of [5] is adapted. Based on the initial field data $\mathbf{F}^{[0]}$, the solution of

$$\hat{\mathbf{I}}^{[i]} = \arg\min_{\tilde{\mathbf{I}}}\left\|\boldsymbol{\Psi}\cdot\tilde{\mathbf{I}} - \mathbf{F}^{[i-1]}\right\|_2 \text{ such that } \mathbf{K}\cdot\tilde{\mathbf{I}} = 0 \tag{17}$$

is determined in the i-th iteration step ($i \in \mathbb{N}^*$). Afterwards, the field data

$$\hat{\mathbf{F}}^{[i]} = \boldsymbol{\Psi}\cdot\hat{\mathbf{I}}^{[i]} \tag{18}$$

of the reconstructed current distribution is calculated. Its phase information is used for the field data in the next iteration step:

$$\mathbf{F}^{[i]} = \left|\mathbf{F}^{[i-1]}\right|\circ\exp\left(\mathrm{j}\cdot\arg\hat{\mathbf{F}}^{[i]}\right) \tag{19}$$

The initial field data $\mathbf{F}^{[0]}$ consists of the measured electric ($\mathbf{E}_\mathrm{mag}$) and magnetic ($\mathbf{H}_\mathrm{mag}$) magnitudes and an initial guess of the phase distribution $\boldsymbol{\varphi}_0$:

$$\mathbf{F}^{[0]} = \left[\alpha_\mathrm{E}\mathbf{E}_\mathrm{mag}\quad \alpha_\mathrm{H}\mathbf{H}_\mathrm{mag}\right]^\mathrm{T}\circ\exp\left(\mathrm{j}\boldsymbol{\varphi}_0\right) \tag{20}$$

In difference to [5], $\boldsymbol{\varphi}_0$ is not chosen as uniformly distributed phase in this work. In the following chapter, the used approach is presented.

Two criterions are defined to formulate a termination condition for the iterative algorithm. In the first criterion, the mean absolute relative deviation of the inverse problem solution is evaluated [5]:

$$\sigma_{\Delta I}^{[i]} = \frac{1}{\mathrm{K_I}}\sum_{k=1}^{\mathrm{K_I}}\left|\frac{\hat{I}_k^{[i]} - \hat{I}_k^{[i-1]}}{\hat{I}_k^{[i]}}\right|, \quad \hat{\mathbf{I}}^{[i]} = \left[\hat{I}_k^{[i]}\right]_{k=1,\dots,\mathrm{K_I}} \tag{21}$$

Here, $\mathrm{K_I}$ is the number of elements in $\hat{\mathbf{I}}^{[i]}$. Using the second criterion, the deviation of the reconstructed phase information of the near-field is rated. It is determined with the mean absolute value of the minimal phase deviation:

$$\begin{aligned} \sigma_{\Delta\varphi}^{[i]} &= \frac{1}{\mathrm{K}_\varphi}\sum_{k=1}^{\mathrm{K}_\varphi}\min\left\{\left|\Delta\varphi_k^{[i]}\right|, 2\pi - \left|\Delta\varphi_k^{[i]}\right|\right\}, \\ \left[\Delta\varphi_k^{[i]}\right]_{k=1,\dots,\mathrm{K}_\varphi} &= \arg\hat{\mathbf{F}}^{[i]} - \arg\hat{\mathbf{F}}^{[i-1]} \end{aligned} \tag{22}$$

Here, K_φ is the number of elements in $\hat{\mathbf{F}}^{[i]}$. In this paper, the following termination condition is used to abort the iterative algorithm:

$$\left(\sigma_{\Delta I}^{[i]} < 1‰\right)\wedge\left(\sigma_{\Delta\varphi}^{[i]} < 2\pi/1000\right) \tag{23}$$

D. Refined Constrains About Terminations

Appling the iterative algorithm, its solution primarily satisfies the minimization of the mathematic residua. So, the solution may not fit the actual physics. One of these rules handles passive termination networks. Generally, if the k-th section is terminated with a passive network, its complex impedance $Z_{\mathrm{T},k}$ must fulfil the condition

$$0 \le \operatorname{Re}\left\{Z_{\mathrm{T},k}\right\}. \tag{24}$$

This is rephrased by the complex power $S_{\mathrm{T},k}$ that is delivered to the termination network. This power can be represented by the current $I_{\mathrm{T},k}$ floating into the termination network:

$$S_\mathrm{T,k} = Z_\mathrm{T,k}\cdot\left|I_\mathrm{T,k}\right|^2 \tag{25}$$

So, the condition of (24) is fulfilled if active power $P_{\mathrm{T},k}$ is dissipated in the passive termination network:

$$0 \le \operatorname{Re}\left\{Z_{\mathrm{T},k}\right\} \overset{|I_{\mathrm{T},k}|\neq 0}{=} \operatorname{Re}\left\{\frac{S_{\mathrm{T},k}}{\left|I_{\mathrm{T},k}\right|^2}\right\} = \frac{P_{\mathrm{T},k}}{\left|I_{\mathrm{T},k}\right|^2} \tag{26}$$

According to [10], based on this active power, a condition using the incident and reflected current waves $I_{\mathrm{i},k}$ and $I_{\mathrm{r},k}$ can be formulated:

$$\begin{aligned} \Rightarrow 0 \le P_{\mathrm{T},k} &= |a_k|^2 - |b_k|^2 = |a_k|^2\left(1-|r_k|^2\right) \\ &= |a_k|^2/\left|I_{\mathrm{i},k}\right|^2\left(\left|I_{\mathrm{i},k}\right|^2 - \left|I_{\mathrm{r},k}\right|^2\right) \end{aligned} \tag{27}$$

$$\Leftrightarrow 1 \le \left|I_{\mathrm{i},k}\right|/\left|I_{\mathrm{r},k}\right| \tag{28}$$

Here, the incident and reflected power waves are a_k and b_k and the reflection coefficient r_k of the k-th section is used. To use condition (28) as constrain for an inverse problem, the vector

$$\mathbf{c}(\mathbf{I}) = \left[\,1 - \left|I_\mathrm{i,k}\right|/\left|I_\mathrm{r,k}\right|\,\right]_{k\in\mathbb{K}} \tag{29}$$

is formulated. The set $\mathbb{K}$ includes the sections that are described by the transmission-line theory and terminated by a passive network. So, the solution of the representative inverse problem

$$\hat{\mathbf{I}} = \arg\min_{\tilde{\mathbf{I}}}\left\|\boldsymbol{\Psi}\cdot\tilde{\mathbf{I}} - \mathbf{F}\right\|_2 \text{ such that } \begin{cases}\mathbf{K}\cdot\tilde{\mathbf{I}} = \mathbf{0} \\ \mathbf{c}(\tilde{\mathbf{I}}) \le \mathbf{0}\end{cases} \tag{30}$$

considers (28) for all passive termination networks. Here, in the constraint, the inequation must be fulfilled for each component.

Also, the condition (28) can be used to choose an initial phase distribution for the iterative algorithm. To do so, a current (wave) vector $\mathbf{I}_\mathrm{rand}$ of the inverse problem is chosen.

In this vector, all incident current waves $I_{\mathrm{i},k}$ ($k \in \mathbb{K}$) are random with normal distributed magnitudes and uniformly distributed phases:

$$I_{\mathrm{i},k} = n_1 \cdot \exp(\mathrm{j}n_2), \quad n_1 \sim \mathcal{N}(0,1), \; n_2 \sim \mathcal{U}(0,2\pi) \tag{31}$$

Accordingly, the reflected current waves are defined as

$$I_{\mathrm{r},k} = I_{\mathrm{i},k} \cdot n_3 \cdot \exp(\mathrm{j}n_4), n_3 \sim \mathcal{U}(0,1), n_4 \sim \mathcal{U}(0,2\pi). \tag{32}$$

Using the uniformly distributed scalar n_3, the central condition (28) is fulfilled. In addition, the uniformly distributed factor n_4 ensures many possible current distributions. The entries of $\mathbf{I}_{\mathrm{rand}}$ for the sections carrying a constant current ($k \notin \mathbb{K}$) are assumed to be zero. So, the information on the power flow's correct direction is considered in the initial guess of the phase distribution:

$$\boldsymbol{\varphi}_0 = \arg(\boldsymbol{\Psi} \cdot \mathbf{I}_{\mathrm{rand}}) \tag{33}$$

E. Evaluation of the Reconstruction Result

In this work, two further evaluation approaches are applied to the reconstruction result. Firstly, the reconstructed incident and reflected waves are used to determine the termination impedance or input impedance of a section described by the transmission-line theory [8]. For example, for section k_2 in Fig. 1, the input impedance is given by

$$Z_{\mathrm{in,k}_2} = Z_{0,\mathrm{k}_2} \left(I_{\mathrm{i,k}_2} + I_{\mathrm{r,k}_2}\right) / \left(I_{\mathrm{i,k}_2} - I_{\mathrm{r,k}_2}\right), \tag{34}$$

where Z_{0,k_2} denotes the wave impedance.

The second approach uses Hertzian dipoles as segments to predict the electric field on the basis of the reconstructed current distribution [5].

III. Application to Measurement Data

A. Case Study Object

A simple three wire system is used as case study. It is assumed, that the electric field at a specified point must be reduced. To do so, the electromagnetic near-field is used to locate the critical field sources.

The investigated structure is shown in Fig. 1. In Fig. 2, a top is presented. The used copper wire radius is 0.25 mm and their height above the copper plane is 2 mm. In Fig. 2, the wire excitation ports are represented by the numbered ends. All other ends are terminated with a parallel circuit of an 100 kΩ resistor and a 10 pF ceramic capacitor each. The vector network analyzer (VNA) KEYSIGHT (AGILENT) E5071B is used for the structure's excitation and the near-field measurement. The structure is excited at ports 1-3, the sources have an internal resistance of 50 Ω. A near-field probe is connected to port 4 of the VNA. Here, for wire 1 and 2, an excitation of 1 V is chosen. Wire 3 is stimulated with 4 V. All sources are in phase. Using the determined power at port 4, the available phase information is rejected. The magnetic field is measured by the active near-field probe MFA-R 0.2-75 from LANGER EMV. To determine the electric field, the passive near-field probe RS-E 10 from RHODE & SCHWARZ is used. The field is measured at the 46 points depicted in Fig. 2 7 mm above the ground plane. Investigating the frequency range from 50 MHz to 250 MHz with a step size of 50 MHz, for all points, the field components H_{x}, H_{y} and E_{z} are measured.

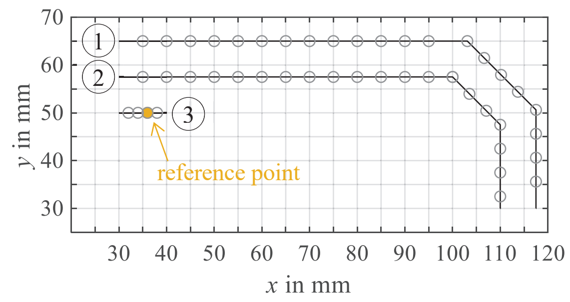

Fig. 2. Investigated structure with wires and wire numbers; positions of the measurement points (circles).

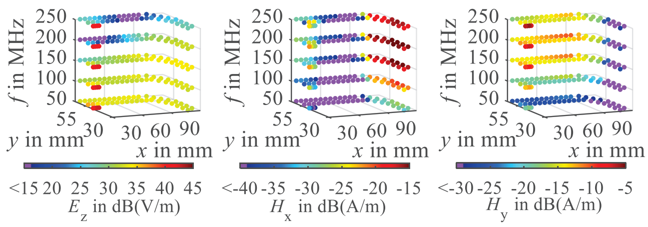

Fig. 3. Measured absolute field strengths.

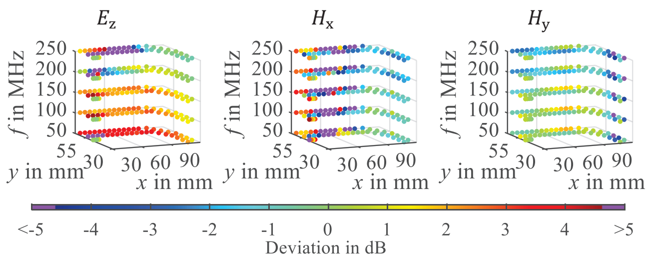

Fig. 4. Deviation of the measured field strengths from simulation data.

To calibrate the setup and generate the reference data, the structure is simulated in CONCEPT-II [11]. Due to the chosen excitation, high field strengths can be expected for the filled reference point in Fig. 2. So, at this point, the simulated field strengths H_{y} and E_{z} are used to calibrate the used near-field probes. Also, the phase of H_{y} at this point is used to refer the reconstructed phase information.

In Fig. 3, the measured near-field data is shown. To highlight the measurement data's dynamic, datapoints having a field strength below a specific threshold are marked violet. The deviation of the measured data from the simulation data is presented in Fig. 4. Here, deviations above ± 5 dB are also marked in violet. Generally, for data points with high magnetic field strength, the deviation is in the range of 2 dB. The electric field shows a larger deviation. This can be explained by an imprecisely positioned field probe.

Determining critical sources in this structure, a simple approach is to search for hot spots (i.e. high field strengths) in the near-field. In this case, wire 3 appears to be critical. However, in the following investigation, it is shown that the simple search for hot spots leads to wrong conclusions.

B. Reconstruction of the Current Distribution

Finally, the current distribution is reconstructed. The structure is discretized in segments having a length of 1 mm or smaller. So, the used reconstruction model includes 247 elements. Using the presented iterative algorithm, the current distribution is reconstructed for 50 different initial phase distributions. Also, the condition (28) is considered in the inverse problem. In Fig. 5, the developments of the termination criterions (21) and (22) are presented. In this and the following figures, the results are presented in transparent curves. So, the overlap and its increasing color intensity mark a high occurrence of a solution. Generally, for the most evaluations, the iterative algorithm's termination criterions show a convergent behavior. However, the continuously descending character of the criterions' development is interrupted for some iterations. The usage of the nonlinear constrain (28) may be an explanation for this phenomenon.

Exemplary results of the reconstructed current distributions for 50 MHz, 100 MHz and 150 MHz are shown in Fig. 6. For wire 1 and 2, the absolute values of the reconstructed current distributions have only minor deviations from the simulated current distribution. The solutions for the current distribution of wire 3 show a larger variation, but the deviation from the simulation results is smaller than 2 dB. The error of the reconstructed phase is negligible for wire 3. For wire 2, the deviation of the reconstructed phases is below 40 ° for the most results. The error of the reconstructed phase of wire 1 is in the range from 40 ° to 90 °. This increasing error could be explained with the increasing distance between the currents and the reference point. According to the increasing distance, the field strength of the generating current is fading away. Reciprocally, the reference point's defining character to indicate the phase is also fading.

C. Evaluation of the Field Emission

In this section, the reconstruction results are used to locate sources with critical field emission. For this purpose, similar to an antenna measurement, the field is investigated in an exemplary point. Here, the field at $(x = 0, y = 1, z = 0.1)$ m, Fig. 2, is calculated with an infinite PEC ground plane at $z = 0$. To identify every wire's character as critical source, its contribution to the field is estimated. To do so, the field of a wire is determined isolated from the other wires. According to the number of applications of the iterative algorithm, there are 50 results for each frequency. These estimations for the contributions of the wires to the vertical and horizontal field are shown in Fig. 7. Here, related to the simulated field in CONCEPT-II, the estimated field contributions are presented in transparent colors. In addition, the mean values of the estimations and every wires' simulated contribution to the field are shown.

Generally, the estimation of the field contribution of each wire is close to the simulated contribution. The deviation is below 5 dB. In any case, the qualitative relation of the contributions is determined. Except the evaluations for 50 MHz, also the estimated quantitative values are very accurate. This investigation points out that wire 1 and 2 are probable critical sources for the horizontal and for the vertical electric field at the investigated point. It is possible, that the phase of these wires' current is reverse. So, the emitted field could be compensated. However, the phase is not determined here. Therefore, the field emission of wire 1 and 2 must be suppressed to reduce the whole field emission.

D. Virtual Design of a Filter Concept

After the identification of wire 1 and 2 as probable critical sources, a filter is designed to reduce the field. Here, capacitors are implemented at the stimulated ends of wire 1 and 2. This is shown in Fig. 8. In CONCEPT-II the capacitors are loads in additional wire segments parallel to the vertical wire segments. Here, a minimal capacity is needed for the

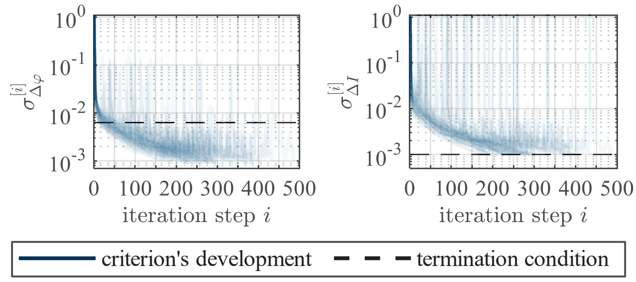

Fig. 5. Development of termination criterions of 50 exemplary runs of the iterative algorithm and termination condition according to (23).

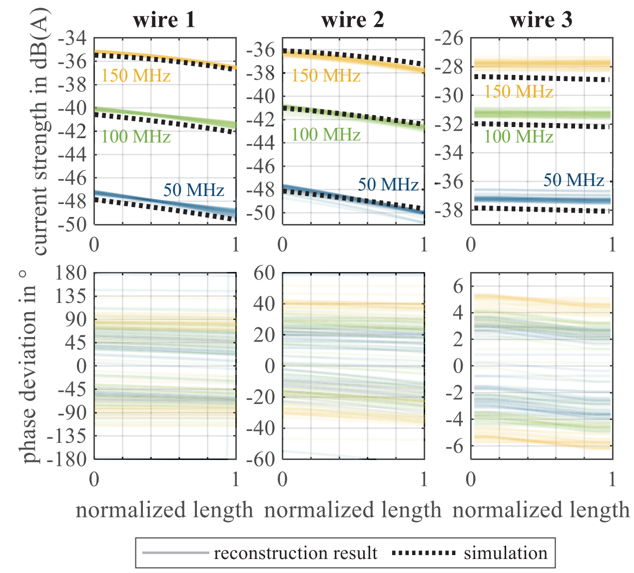

Fig. 6. Exemplary results for the reconstructed current distribution.

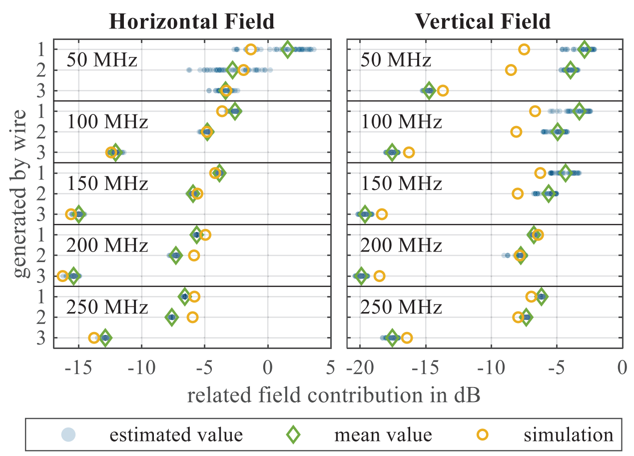

Fig. 7. Contributions of the wires to the electrical field related to the simulated field of the whole structure.

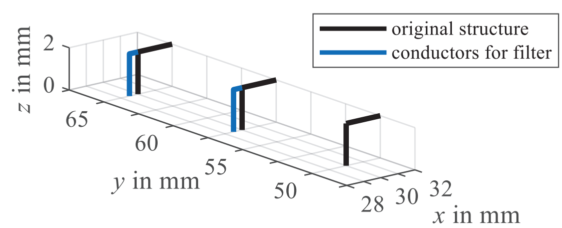

Fig. 8. Wires parallel filter structure to reduce the field emission.

filters to reduce the impact on signals with lower frequencies. For finding a proper capacitor value, based on the reconstructed current distribution, the wire input impedances are calculated. In Fig. 9, the results are presented.

In the frequency range from 50 MHz to 150 MHz, the capacitive character of the wire termination is represented. For 200 MHz, a very small value for the input impedance is noticeable. Considering the quasi-static character of the wire system for this frequency, the inductance of the wire and its termination show resonance effects. The estimated higher value for the impedance for 250 MHz proves this hypothesis.

The filter capacitors' impedance $|Z_{\mathrm{C}}|$ is selected so that their impedance is smaller than the input impedance of the wires by a factor of 10. Since the input impedance of the wires is approximately 400 Ω at 50 MHz, the filter capacitance can be calculated according to:

$$|Z_{\mathrm{C}}| = \frac{1}{\omega C}\bigg|_{f=50\,\mathrm{MHz}} \overset{!}{<} \frac{400\,\Omega}{10} \Rightarrow C \gtrsim 80\,\mathrm{pF} \qquad (35)$$

So, 80 pF capacitors are selected for filtering. Additional, 10 Ω resistors are serially connected to mitigate resonance phenomena. The electric field is simulated in CONCEPT-II. In a further simulation, the field is determined with a deactivated excitation for wire 3. The simulated fields are presented in Fig. 10.

It is found that deactivating the excitation of wire 3 has a negligible effect on the field. However, the implemented filtering capacitors (with the serial resistors) reduce the emitted field significantly. Only at approximately 200 MHz, the filters have no positive effect due to resonance effects. It can also be found that the analysis based on the current reconstruction is reasonable to locate critical field sources. The approach is also useful to design suitable filters.

IV. Conclusion and Outlook

In this paper, a current reconstruction method based on near-field data is enhanced by two important features: First, not only the magnetic field is considered, but also the electric field is taken into account. Both fields are used to reconstruct the current distributions of known wire structures. Second, referring to passive termination networks, a basic condition about the power flow is presented. Using this condition, more reasonable initial values can be estimated to find better amplitude and phase distributions. This condition can also be used as a powerful constrain for the inverse problem.

With the help of a simple configuration of three wires, the improved method has been analyzed. Here, near-field data has been measured and evaluated. Both enhancements enable better reconstruction results for the current distribution. This could be shown by simulations. Using the found total current distribution along the wires, the actual critical wires could be found. As the current density in the analyzed configuration is low, it would have been impossible to identify the sources only by looking at the near-field data. Also, based on the reconstruction results, an approach has been presented to design a suitable filtering circuit.

The presented application is a rather simple, academic configuration. Next, more complex structures like traces on real PCBs should be investigated. Additionally, the reconstruction method should be enhanced to improve the phase determination. So, it could be possible to identify compensating field sources.

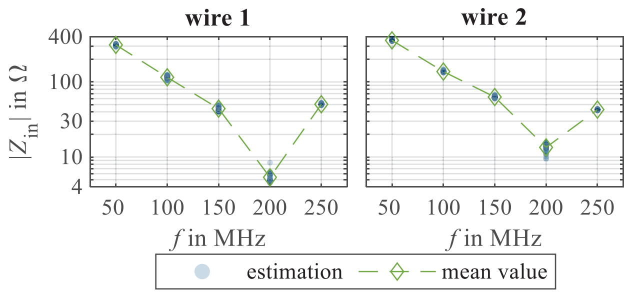

Fig. 9. Absolute value of the determined input impedance.

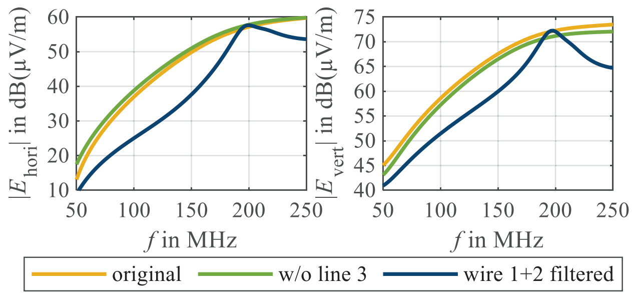

Fig. 10. Investigated simulated electric field from original structure and filtered configurations.

References

[1] X. Gao, J. Fan, Y. Zhang, H. Kajbaf and D. Pommerenke, "Far-Field Prediction Using Only Magnetic Near-Field Scanning for EMI Test," IEEE Trans. Electromagn. Compat., vol. 56, no. 6, pp. 1335-1343, May 2014.

[2] Q. Huang *et al*., "MoM-Based Ground Current Reconstruction in RFI Application," in *IEEE Transactions on Electromagnetic Compatibility*, vol. 60, no. 4, pp. 1121-1128, Aug. 2018.

[3] P. Maheshwari, H. Kajbaf, V. V. Khilkevich and D. Pommerenke, "Emission Source Microscopy Technique for EMI Source Localization," in *IEEE Transactions on Electromagnetic Compatibility*, vol. 58, no. 3, pp. 729-737, June 2016.

[4] R. Takeda and T. Aoyagi, "Development of Near-Field Source Localization Method using Convolutional Neural Network," *2019 Joint International Symposium on Electromagnetic Compatibility, Sapporo and Asia-Pacific International Symposium on Electromagnetic Compatibility (EMC Sapporo/APEMC)*, Sapporo, Japan, 2019, pp. 686-689.

[5] R. Nowak and S. Frei, "Reconstruction of Current Distribution on a Given Conductor Structure Using Frequency Domain Near-Field Data without Phase Information," *2019 International Symposium on Electromagnetic Compatibility (EMC EUROPE*,) Barcelona, 2019, pp. 668-673

[6] H. Zhao, S. Tao, Z. Chen and J. Hu, "Sparse Source Model for Prediction of Radiations by Transmission Lines on a Ground Plane Using a Small Number of Near-Field Samples," in *IEEE Antennas and Wireless Propagation Letters*, vol. 18, no. 1, pp. 103-107, Jan. 2019.

[7] Z. Yu, J. A. Mix, S. Sajuyigbe, K. P. Slattery and J. Fan, "An Improved Dipole-Moment Model Based on Near-Field Scanning for Characterizing Near-Field Coupling and Far-Field Radiation From an IC," in *IEEE Transactions on Electromagnetic Compatibility*, vol. 55, no. 1, pp. 97-108, Feb. 2013.

[8] R. Nowak and S. Frei, "Reconstruction of Current Distribution and Termination Impedances of PCB-Traces by Magnetic Near-Field Data and Transmission-Line Theory," *2018 International Symposium on Electromagnetic Compatibility (EMC EUROPE)*, Amsterdam, 2018, pp. 579-584

[9] C. A. Balanis, *Advanced Engineering,* 2nd ed. New York, NY, USA: Wiley, 2012.

[10] R. Mavaddat, *Network Scattering Parameters*. Singapore: World Scientific Publishing Co. Pte. Ltd., 1996.

[11] *CONCEPT-II*. (2019). Institute of Electromagnetic Theory, Hamburg University of Technology. Available: http://www.tet.tuhh.de/concept/